

# Magnetotransport Trends in Epitaxial Films and Electronic Devices of Correlated Layered Ruthenate $\text{Sr}_3\text{Ru}_2\text{O}_7$

Prosper Ngabonziza,<sup>1,2,\*</sup> Anand Sharma,<sup>1</sup> Anna Scheid,<sup>3</sup>  
Sethulakshmi Sajeev,<sup>1</sup> Peter A. van Aken,<sup>3</sup> and Jochen Mannhart<sup>3</sup>

<sup>1</sup>*Department of Physics & Astronomy, Louisiana State University, Baton Rouge, LA 70803, USA*

<sup>2</sup>*Department of Physics, University of Johannesburg,*

*P.O. Box 524 Auckland Park 2006, Johannesburg, South Africa*

<sup>3</sup>*Max Planck Institute for Solid State Research, Heisenbergstr. 1, 70569 Stuttgart, Germany*

(Dated: October 23, 2023)

For epitaxial  $\text{Sr}_3\text{Ru}_2\text{O}_7$  films grown by pulsed laser deposition, we report a combined structural and magnetotransport study of thin films and Hall bar devices patterned side-by-side on the same film. Structural properties of these films are investigated using X-ray diffraction and high-resolution transmission electron microscopy, and confirm that these films are epitaxially oriented and nearly phase pure. For magnetic fields applied along the  $c$ -axis, large positive magnetoresistance up to 40% and 140% are achieved in unpatterned  $\text{Sr}_3\text{Ru}_2\text{O}_7$  films and Hall bar devices, respectively. These films show switching behaviors from positive to negative magnetoresistance that are controlled by the direction of the applied magnetic field. The present results provide a promising route for achieving stable epitaxial synthesis of intermediate members of correlated layered strontium ruthenates, and for the exploration of device physics in thin films of these compounds.

## 1. Introduction

Layered ruthenates are peculiar strongly correlated materials in which several comparable interactions compete to give rise to a variety of novel electronic and magnetic phenomena. Intricate phenomena observed in layered ruthenates range from superconductivity [1] to emergent ferromagnetism and insulator-metal transitions [2], to colossal and large magnetoresistance [3], and other electron- and spin-ordering states [4]. The layered strontium ruthenates of the Ruddlesden-Popper (R-P) phases,  $\text{Sr}_{n+1}\text{Ru}_n\text{O}_{3n+1}$  ( $n = 1, 2, 3, \infty$ ), play a pivotal role in the study of strongly correlated electron systems. Depending on the number  $n$  of the  $\text{RuO}_6$  octahedra layers in the unit cell, the phenomena obtained in these systems include potentially unconventional superconductivity in  $\text{Sr}_2\text{RuO}_4$  ( $n = 1$ ) [1, 5–7], metamagnetic quantum criticality and electron nematic fluid in  $\text{Sr}_3\text{Ru}_2\text{O}_7$  ( $n = 2$ ) [8–11], orbital-dependent double metamagnetic transition and characteristics of Hund’s metal correlations in  $\text{Sr}_4\text{Ru}_3\text{O}_{10}$  ( $n = 3$ ) ( $n=3$ ) [12–15], and itinerant ferromagnetism coexisting with localized correlated behavior in  $\text{SrRuO}_3$  ( $n = \infty$ ) [16–19]. The rich array of distinct collective phenomena in these materials show that  $\text{Sr}_{n+1}\text{Ru}_n\text{O}_{3n+1}$  are attractive for exploring the rich physics of strongly correlated layered materials.

Beyond fundamental interests, the potential of  $\text{Sr}_{n+1}\text{Ru}_n\text{O}_{3n+1}$  for applied physics has driven interests in thin films, particularly in  $\text{Sr}_2\text{RuO}_4$  ( $n = 1$ ) films due to its unconventional superconductivity and Shubnikov–de Haas effect [20, 21], and in  $\text{SrRuO}_3$  ( $n = \infty$ ) films as an excellent electrode material integrated in diverse oxide thin-film devices for a variety of oxide electronic

and nanoionic applications [16, 22], and also as a candidate Weyl semimetal magnetic material [23, 24]. However, due to the complexity of synthesizing phase-pure epitaxial films of intermediate  $\text{Sr}_{n+1}\text{Ru}_n\text{O}_{3n+1}$  members ( $1 < n < \infty$ ), only a few publications reported attempts to epitaxially grow double- and triple-layered strontium ruthenate films,  $\text{Sr}_3\text{Ru}_2\text{O}_7$  and  $\text{Sr}_4\text{Ru}_3\text{O}_{10}$  [10, 25]. Understanding the synthesis science of epitaxial films of these intermediate members provide a unique opportunity for further explorations of their correlated phases in thin films and electronic devices. Also, the precise control of their functional interfaces at the atomic level will open new routes towards the realization of novel interface-induced functionalities in correlated layered ruthenates, which would otherwise not be accessible when using single crystals.

We focus on epitaxial films of the bilayer strontium ruthenate  $\text{Sr}_3\text{Ru}_2\text{O}_7$ . The material  $\text{Sr}_3\text{Ru}_2\text{O}_7$  is an enhanced Pauli paramagnet in its ground state that undergoes an anisotropic metamagnetic transition (*i.e.*, a sudden increase in the magnetization within a small change of applied magnetic field) [26, 27]. Under magnetic field applied in the out-of-plane direction,  $\text{Sr}_3\text{Ru}_2\text{O}_7$  displays unusual double metamagnetic transitions at critical magnetic fields of  $\sim 8$  T and 13.5 T [28]. However, for in-plane magnetic fields parallel to the ruthenium oxygen planes, metamagnetic behaviors shift to a lower critical field of  $\sim 5.5$  T [27]. In magnetotransport, a peak in the magnetoresistance (MR) has been observed around 5T under in-plane applied magnetic fields, and it has been attributed to originate from in-plane metamagnetic behavior of  $\text{Sr}_3\text{Ru}_2\text{O}_7$  [10, 29, 30]. Metamagnetic transitions in double- and triple-layered ruthenates have been proposed to arise from magnetic fluctuations due to the presence of flat bands near the Fermi level in the electronic band dispersions [15, 31–35]. Also, electron nematic behaviors [36], ascribed to a spin-dependent symmetry-

\* corresponding author: [pngabonziza@lsu.edu](mailto:pngabonziza@lsu.edu)

breaking Fermi surface distortion, have been observed both in single crystals and strained epitaxial films of  $\text{Sr}_3\text{Ru}_2\text{O}_7$  [8, 10, 29].

Although magnetotransport properties of  $\text{Sr}_3\text{Ru}_2\text{O}_7$  have been characterized both in bulk single crystals [37], single crystalline nanosheets [30], and in compressively-strained epitaxial films [10], little is known about the MR characteristics of epitaxial  $\text{Sr}_3\text{Ru}_2\text{O}_7$  films and thin-film devices patterned side-by-side on the same film. Such epitaxial films are ideal for the exploration of lateral dimensional confinement effects in epitaxial films for tuning their electronic ground states. Also, having various micro- and nano-scale devices fabricated side-by-side on the same film provides an advantage over single crystal-based devices, because it provides the opportunity to perform comparative study of magnetotransport properties from the same sample, measured in similar conditions.

In this work, we report on the epitaxy of  $\text{Sr}_3\text{Ru}_2\text{O}_7$  thin films, as well as on the magnetotransport trends of epitaxial films and electronic devices of  $\text{Sr}_3\text{Ru}_2\text{O}_7$ . The synthesis of near phase-pure  $\text{Sr}_3\text{Ru}_2\text{O}_7$  films was previously reported, but only for epitaxial films grown by molecular beam epitaxy (MBE) [10, 25]. Here, we use pulsed laser deposition (PLD) for the epitaxial growth of these thin films. First, we focus on optimizing the PLD growth conditions for achieving phase-pure epitaxial  $\text{Sr}_3\text{Ru}_2\text{O}_7$  films. Subsequent structural analyses of these samples, using x-ray diffraction (XRD) and high-resolution scanning transmission electron microscopy (STEM), confirm that these films are epitaxially oriented and nearly phase pure. From magnetization characterization, the  $\text{Sr}_3\text{Ru}_2\text{O}_7$  films show no ferromagnetic transition over the entire measured temperature range. Second, for epitaxial films prepared at optimal growth conditions, we fabricate side-by-side on the same  $\text{Sr}_3\text{Ru}_2\text{O}_7$  sample several Hall bar devices of various channel widths, to then explore their electronic transport properties. We find that the sheet resistance of Hall bar devices increases as the active channel width of  $\text{Sr}_3\text{Ru}_2\text{O}_7$  films decreases, while the sheet resistance of unpatterned films is higher than those of structured Hall bar devices. Lastly, we perform a comparative MR study of unpatterned epitaxial  $\text{Sr}_3\text{Ru}_2\text{O}_7$  films and Hall bar devices. At low temperatures, for magnetic fields applied along the  $c$ -axis ( $B \parallel c$ ), with the excitation current perpendicular to the direction of applied field, we observe negative MR behavior of 40% in unpatterned films and enhanced negative MR up to 140% in patterned Hall bar devices. Furthermore, these films show switching behaviors from positive to negative MR that are controlled by the direction of the applied magnetic field

## 2. Thin Film Epitaxy

Figure 1(a) illustrates the epitaxy of  $\text{Sr}_3\text{Ru}_2\text{O}_7$  films on a  $\text{TiO}_2$ -terminated  $\text{SrTiO}_3$  substrate. All  $\text{Sr}_3\text{Ru}_2\text{O}_7$  films were grown on (100)-oriented  $\text{SrTiO}_3$  single crystalline substrates ( $5 \times 5 \times 1 \text{ mm}^3$ ) [Fig. 1(b)]. Prior to deposition, the  $\text{SrTiO}_3$  substrates were terminated in situ

using a  $\text{CO}_2$  laser [38]. We deposited  $\text{Sr}_3\text{Ru}_2\text{O}_7$  films using PLD by ablating a stoichiometric  $\text{Sr}_3\text{Ru}_2\text{O}_7$  target [39] with an excimer laser ( $\lambda = 248 \text{ nm}$ ) at 2 Hz to a thickness of 25 nm. During growth, the molecular oxygen pressure in the chamber was kept at  $P_{\text{O}_2} = 8.0 \times 10^{-2}$  mbar. Immediately after growth, under the same  $P_{\text{O}_2}$ , samples were cooled to room temperature at a cooling rate of  $80^\circ\text{C}/\text{min}$ . To establish stable epitaxial growth conditions, we have prepared a series of  $\text{Sr}_3\text{Ru}_2\text{O}_7$  films at various substrate temperatures ( $T_{\text{sub}}$ ), from  $680$  to  $800^\circ\text{C}$  in steps of  $20^\circ\text{C}$ . The optimal substrate temperature for the epitaxial growth of  $\text{Sr}_3\text{Ru}_2\text{O}_7$  films was found to be  $T_{\text{sub}} = 720^\circ\text{C}$ . At this temperature, we have also prepared a series of  $\text{Sr}_3\text{Ru}_2\text{O}_7$  films varying the laser fluence from  $1.5$  to  $3 \text{ J}/\text{cm}^2$  in steps of  $0.5 \text{ J}/\text{cm}^2$ , and better quality films were obtained at a laser fluence of  $2.5 \text{ J}/\text{cm}^2$ .

## 3. Results and Discussion

The surface quality of epitaxial  $\text{Sr}_3\text{Ru}_2\text{O}_7$  films was characterized by reflection high-energy electron diffraction (RHEED) and atomic force microscopy (AFM). The deposition of  $\text{Sr}_3\text{Ru}_2\text{O}_7$  was in situ monitored by RHEED [Fig. 1(c)]. We observe that the intensity of time-dependent RHEED oscillations remains roughly the same throughout the deposition of the  $\text{Sr}_3\text{Ru}_2\text{O}_7$  layers on  $\text{SrTiO}_3$  substrates. The RHEED oscillations indicate that the  $\text{Sr}_3\text{Ru}_2\text{O}_7$  films are grown in a layer-by-layer mode with a smooth surface as also demonstrated by sharp, diffracted, and specular RHEED patterns [inset in Fig. 1(c)]. After PLD growth, the surface morphology of the  $\text{Sr}_3\text{Ru}_2\text{O}_7$  films was investigated using AFM. Figure 1(d) depicts a typical AFM image for a representative 25-nm-thick  $\text{Sr}_3\text{Ru}_2\text{O}_7$  film. The surface of the resulting  $\text{Sr}_3\text{Ru}_2\text{O}_7$  films at optimal substrate temperature is smooth and it exhibits well-pronounced terraces, demonstrating a high quality surface morphology of these films. For a lateral scan size of  $\sim 5 \times 5 \mu\text{m}^2$ , the extracted surface roughness is  $\leq 0.2 \text{ nm}$  for a 25-nm-thick  $\text{Sr}_3\text{Ru}_2\text{O}_7$  film [bottom panel in Fig. 1(d)].

The crystalline quality and phase purity of  $\text{Sr}_3\text{Ru}_2\text{O}_7$  films were characterized by XRD. Figure 2(a) shows representative  $\theta - 2\theta$  scans for the  $\text{Sr}_3\text{Ru}_2\text{O}_7$  films at various substrate temperatures and laser fluence. For the films grown at optimal growth conditions ( $T_{\text{sub}} = 720^\circ\text{C}$  and laser fluence =  $2.5 \text{ J}/\text{cm}^2$ ), only the substrate peaks and phase-pure  $00l$  family of the film diffraction peaks are resolved, which indicates a high crystallinity and verifies that the  $\text{Sr}_3\text{Ru}_2\text{O}_7$  films were aligned along the  $c$ -axis. The  $002$ ,  $004$ ,  $008$ ,  $0010$ ,  $0012$ ,  $0014$ ,  $0020$ , and  $0022$  Bragg diffraction peaks are well resolved, while the  $006$ ,  $0016$ , and  $0018$  peaks are not present due to the small film thickness and the low structure factors of these peaks [10]. The extracted out-of-plane lattice parameter for epitaxial films grown at the optimal growth conditions is  $c = 20.72 \text{ \AA}$ . This value is consistent to the bulk  $c$ -axis lattice constant of  $20.7194 \text{ \AA}$  reported previously in single crystals of  $\text{Sr}_3\text{Ru}_2\text{O}_7$  [30, 40–42]. Extra phases,

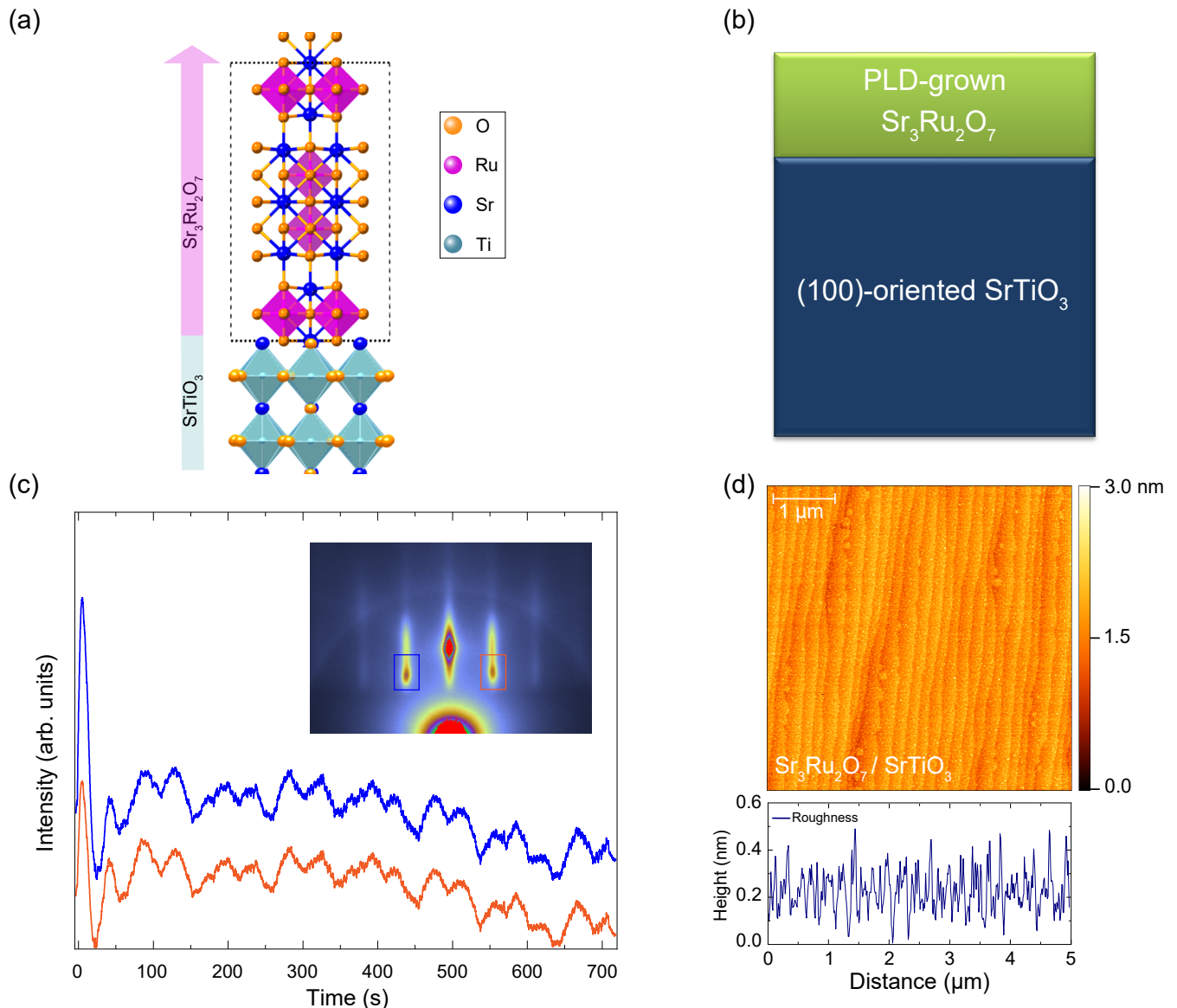


FIG. 1. **Crystal structure and surface quality of epitaxial  $\text{Sr}_3\text{Ru}_2\text{O}_7$  films.** Schematic representation of (a) the crystal structure and (b) layout of the double-layered  $\text{Sr}_3\text{Ru}_2\text{O}_7$  thin film grown by pulsed laser deposition on a (001)-oriented  $\text{SrTiO}_3$  substrate. Dashed-line rectangle in (a) delineates the unit cell of  $\text{Sr}_3\text{Ru}_2\text{O}_7$ . (c) Time-dependent RHEED intensity oscillations recorded during the growth of  $\text{Sr}_3\text{Ru}_2\text{O}_7$ . The inset depicts RHEED patterns of a  $\text{Sr}_3\text{Ru}_2\text{O}_7$  film, where the blue and orange rectangles mark the region from which the integrated intensity as a function of time was recorded during the deposition of  $\text{Sr}_3\text{Ru}_2\text{O}_7$ . (d) A representative AFM image displaying the surface morphology and (bottom panel) corresponding surface roughness profile of a typical  $\text{Sr}_3\text{Ru}_2\text{O}_7$  film.

indicated by (#) in Fig. 2(a), were detected in  $\text{Sr}_3\text{Ru}_2\text{O}_7$  films grown at high substrate temperatures, underlining the role of proper tuning of  $T_{\text{sub}}$  for achieving phase stability in these films.

Figure 2(b) shows a closeup view of the  $\theta - 2\theta$  scans around the  $00\bar{1}0$  diffraction peak for the  $\text{Sr}_3\text{Ru}_2\text{O}_7$  films grown at various  $T_{\text{sub}}$  and laser fluence. For the films grown at the optimal growth conditions, only the  $00\bar{1}0$  peaks are resolved with noticeable thickness fringes, which highlight phase purity and smooth growth. How-

ever, we observed shifting of the  $00\bar{1}0$  peaks to lower  $2\theta$  angles for films that were not grown at the optimal growth conditions. The shifting of the peak demonstrates that the  $c$ -axis lattice constant expands, indicating inter-growth of other  $\text{Sr}_{n+1}\text{Ru}_n\text{O}_{3n+1}$  phases and change of stability of the  $\text{Sr}_3\text{Ru}_2\text{O}_7$  films. In particular, the  $\text{Sr}_3\text{Ru}_2\text{O}_7$  films grown at  $T_{\text{sub}} = 680^\circ\text{C}$  exhibited a peak shoulder around the substrate peak, indicating an inter-growth of the  $\text{SrRuO}_3$  phase [43].

Figure 2(c) shows four reciprocal space maps (RSM)

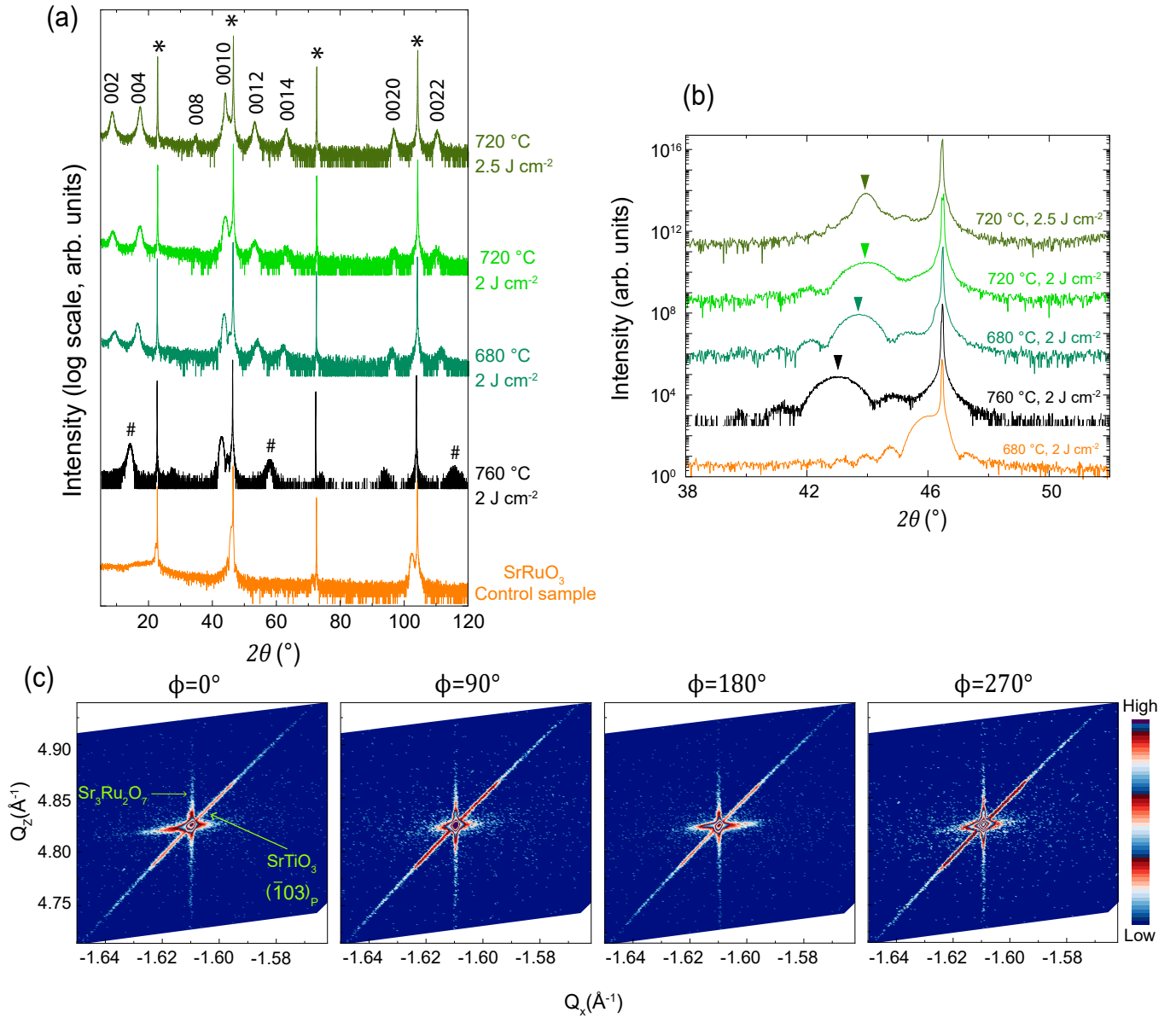


FIG. 2. **Structural characterization of epitaxial  $\text{Sr}_3\text{Ru}_2\text{O}_7$  films.** (a) Representative XRD scans of 25-nm-thick  $\text{Sr}_3\text{Ru}_2\text{O}_7$  films prepared at different growth temperatures and laser fluences together with a scan of a  $\text{SrRuO}_3$  control film (orange curve). For films prepared at optimal substrate temperature (720 °C), only the  $\text{SrTiO}_3$  Bragg's reflection peaks (\*) and the  $00l$  family of the  $\text{Sr}_3\text{Ru}_2\text{O}_7$  films' diffraction peaks are resolved. Extra phases (#) in  $\text{Sr}_3\text{Ru}_2\text{O}_7$  films are observed at high growth temperatures. (b) Closeup XRD patterns around the  $00\bar{1}0$  peak of  $\text{Sr}_3\text{Ru}_2\text{O}_7$ . For growth temperatures higher or lower than 720 °C, the  $00\bar{1}0$  peaks of  $\text{Sr}_3\text{Ru}_2\text{O}_7$  shift to lower values. (c) Reciprocal space maps for a  $\text{Sr}_3\text{Ru}_2\text{O}_7$  film around the  $\bar{1}03_p$  reflection of  $\text{SrTiO}_3$  substrate, where  $p$  refers to pseudocubic indices, measured at four different  $\phi$  angle orientations of the  $\text{SrTiO}_3$  substrate.

around the asymmetric pseudocubic  $\bar{1}03_p$  reflection peak of the substrate for different  $\phi$  angle orientations. From all four RSMs, it is evident that the  $\text{Sr}_3\text{Ru}_2\text{O}_7$  film is fully epitaxially strained and single phase, as confirmed by extracted pseudocubic in-plane lattice constant of  $a = 3.887\text{\AA}$ . This extracted in-plane lattice parameter is consistent with the literature value for single crystals of  $\text{Sr}_3\text{Ru}_2\text{O}_7$  [40, 41]. Although the epitaxial films appear to be single phase from XRD characterization, it

is also essential to use transmission electron microscopy (TEM) to check for inter-growths that are known to be difficult to discern in XRD patterns of layered R-P materials [25, 44, 45].

To provide a complementary real-space microstructural characterization of these films, cross-sectional TEM imaging was performed. With these studies, we investigated the defect populations of these films including possible inter-growths of  $n \neq 2$  members of the

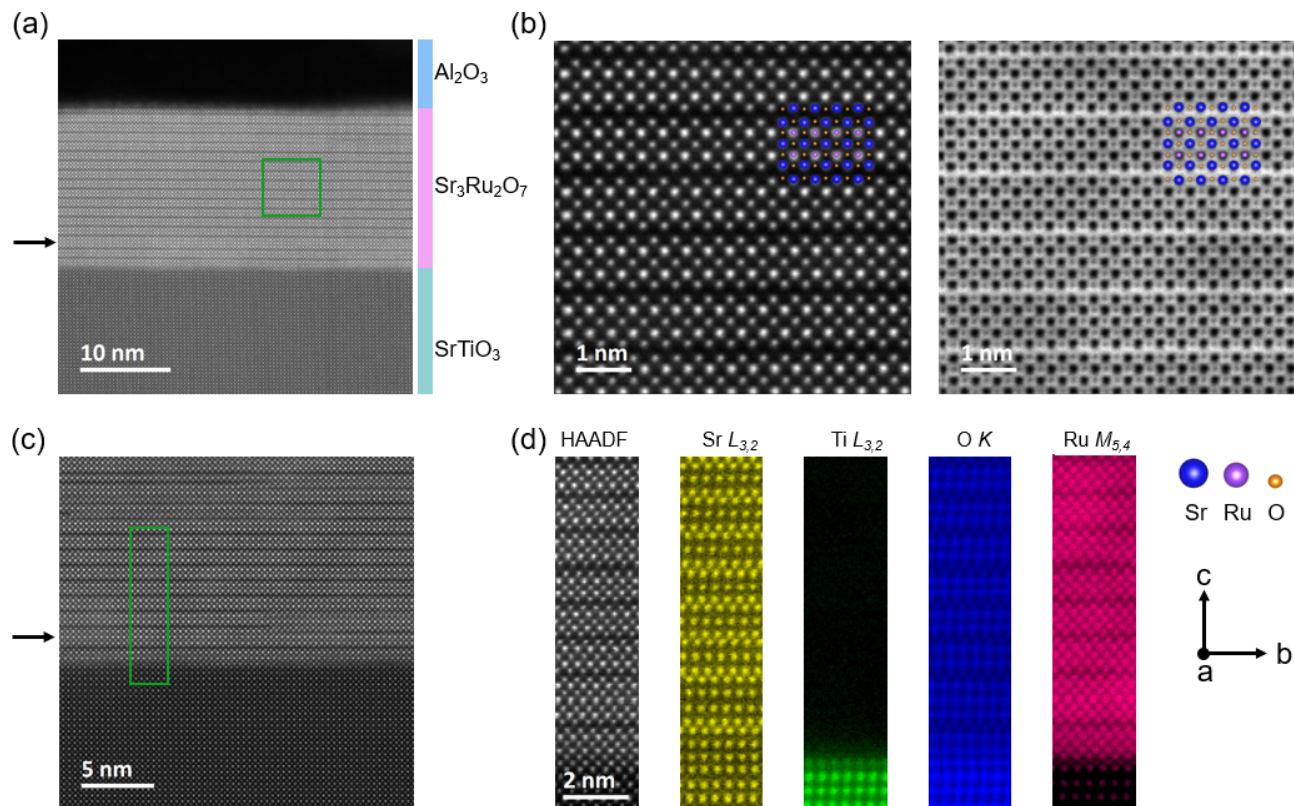


FIG. 3. **Microstructural characterization of representative  $\text{Sr}_3\text{Ru}_2\text{O}_7$  films prepared at optimal growth conditions.** (a) Overview scanning transmission electron microscopy (STEM) image of  $\text{Sr}_3\text{Ru}_2\text{O}_7$  in  $[100]$  zone axis orientation. (b) The magnified annular dark-field (center) and annular bright-field (right) images show the film with a good structural order. A schematic atomic structural model, displaying the sequence of Sr, Ru and O atoms is shown, overlaying the resolved double-layered atomic structure. (c) High-resolution STEM image of a  $\text{Sr}_3\text{Ru}_2\text{O}_7$  film in  $[100]$  orientation together with corresponding (d) electron energy-loss spectroscopy (EELS) elemental mapping of the  $\text{Sr}_3\text{Ru}_2\text{O}_7/\text{SrTiO}_3$  interface showing the elemental distribution in the sample. Due to the overlap of Ru  $M_{4,5}$ -edges with low-intensity Sr  $M_{2,3}$ , residual noticeable Sr signals remain when extracting the Ru signal. Black arrows in (a) and (c) point to regions with  $n = 3$ , which were observed occasionally in films prepared at optimal growth conditions

$\text{Sr}_{n+1}\text{Ru}_n\text{O}_{3n+1}$  series. Figure 3(a) depicts a cross-sectional STEM image of the entire film thickness of a representative  $\text{Sr}_3\text{Ru}_2\text{O}_7$  film prepared at the optimal growth conditions. For films prepared at the optimal substrate temperature, no surface steps at the substrate and defects throughout the entire film thickness were observed. Selected area STEM studies of these films corroborate the epitaxial orientations established by XRD and confirm that the growth occurred along the  $[001]$  direction with the  $c$ -axis out of plane and the films being fully epitaxially strained to the  $\text{SrTiO}_3$  substrate. The STEM images of two representatives  $\text{Sr}_3\text{Ru}_2\text{O}_7$  films distinctly show the double-layered structure of the films, the interface between the substrate and deposited layers being coherent without misfit dislocations along the interface [Figs. 3(a) and 3(c)]. The annular dark-field (center, Fig. 3(b)) and bright-field (right, Fig. 3(b)) images show the Sr and Ru columns with enhanced atomic number contrast. The Ru atomic columns appear brightest due to the much higher atomic number of Ru compared with Sr, as also indicated in the inset with a superimposed

structural model [Fig. 3(b)]. The alternate stacking of the rock salt SrO layers and the  $\text{RuO}_6$  octahedra sheets observed in these images confirms the formation of the desired  $n = 2$  member of the R-P structure. To evaluate the composition of the epitaxial  $\text{Sr}_3\text{Ru}_2\text{O}_7$  films, electron energy-loss spectroscopy (EELS) measurements were performed on the cross section of the samples during STEM characterization. Figure 3(d) displays atomically resolved EELS elemental maps of a  $\text{Sr}_3\text{Ru}_2\text{O}_7$  film. The black color suggests zero intensity, whereas the other colors indicate the expected chemical composition of different elements in the film (Ru, Sr, Ti and O) that are resolved in the scanned region.

For epitaxial  $\text{Sr}_3\text{Ru}_2\text{O}_7$  films grown at optimal growth conditions ( $T_{\text{sub}} = 720^\circ\text{C}$  and laser fluence  $= 2.5 \text{ J/cm}^2$ ), the defects detected are infrequently regions of  $n = 3$  inter-growth within  $n = 2$  layers (indicated by black arrows in Figs. 3(a) and 3(c)). Such inter-growths were found in localized regions with insufficiently ordered volume to give rise to detectable diffraction spots in the XRD patterns. Similar inter-growth of extra  $n$ -

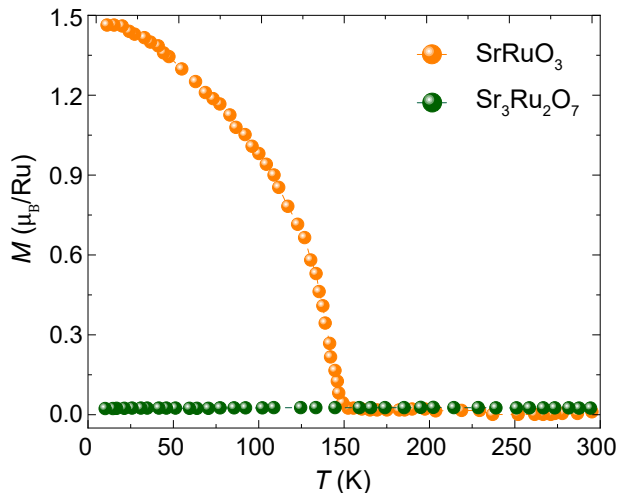


FIG. 4. **Magnetic ground state of Sr<sub>3</sub>Ru<sub>2</sub>O<sub>7</sub> films.** Magnetization as a function of temperature of a typical Sr<sub>3</sub>Ru<sub>2</sub>O<sub>7</sub> film prepared at optimal growth conditions. For comparison, the magnetization data of a SrRuO<sub>3</sub> film is also presented.

phases in R-P layers were reported in epitaxial films of Sr<sub>*n*+1</sub>Ru<sub>*n*</sub>O<sub>3*n*+1</sub> and Sr<sub>*n*+1</sub>Ti<sub>*n*</sub>O<sub>3*n*+1</sub> (*n* = 2 to 5) grown by MBE [10, 25, 44, 46]. STEM investigations of films grown outside the optimal substrate temperature window showed increased defect density and populations of inter-growths of other *n*-phases of the R-P series [See Fig. S1 of the supplementary material]. These inter-growths are difficult to control in epitaxial growth using PLD. This is because minor stoichiometric deviations that can exist between the target and deposited films, together with the fact that the difference in the formation energies among nearby *n* members of the Sr<sub>*n*+1</sub>Ru<sub>*n*</sub>O<sub>3*n*+1</sub> series is small, could lead to the formation of mixed *n*-phase films of these materials [45].

Magnetization as a function of temperature,  $M(T)$ , of Sr<sub>3</sub>Ru<sub>2</sub>O<sub>7</sub> films were studied using a physical property measurements systems (PPMS) vibrating sample magnetometer (VSM). The film was first pre-cooled to 5 K while in a 0.1 T, and then warmed to 300 K in the presence of 0.01 T, the  $M(T)$  data were collected. Figure 4 depicts the  $M(T)$  curve (green) of a representative Sr<sub>3</sub>Ru<sub>2</sub>O<sub>7</sub> film grown on SrTiO<sub>3</sub> at the optimal growth conditions. These magnetization data are obtained after the subtraction of the diamagnetic contribution from the SrTiO<sub>3</sub> substrate. The Sr<sub>3</sub>Ru<sub>2</sub>O<sub>7</sub> films show no ferromagnetic transition, as the  $M(T)$  curve is nearly flat in the measured temperature range. This observation is in agreement with previous reports on the magnetic ground state of single crystals and epitaxial films of this material [25, 26]. However, as it was expected, the  $M(T)$  data of a SrRuO<sub>3</sub> control film prepared in the same PLD chamber show robust ferromagnetic ordering, as revealed by a sharp paramagnetic to ferromagnetic transition at round 150 K, in agreement with previous reports [16, 25, 47].

Now we turn to device fabrication and electronic transport characteristics of epitaxial Sr<sub>3</sub>Ru<sub>2</sub>O<sub>7</sub> films prepared at the optimal growth conditions. To investigate the magnetotransport properties in these films and patterned devices, we fabricated side-by-side on the same film a series of Hall bar devices of various channel widths (from 10 μm to 500 nm) [Fig. 5(a)]. The devices were patterned using electron-beam lithography (EBL) followed by ion-beam etching and the deposition of Ti/Au (5 nm/45 nm) electrodes. Figures 5(b) and 5(c) show top-view scanning electron microscopy (SEM) images of patterned Hall bar devices and a schematic side view of a device together with transport measurement configuration, respectively. Unpatterned Sr<sub>3</sub>Ru<sub>2</sub>O<sub>7</sub> films were measured in a Van der Pauw configuration by wire bonding aluminum wires to the samples' corners. Electronic transport characteristics of patterned thin-film devices, which were fabricated side-by-side on the same film after transport measurements in a Van der Pauw geometry, were studied in a Hall bar configuration with aluminum wires connected to the electrodes [Fig. 5(d)]. For magnetotransport measurements, we used a Quantum Design PPMS operated at 300–5 K. An excitation current of 1 μA was applied. The MR measurements were performed with the magnetic field ( $B$ ) oriented both along the  $c$ -axis ( $B \parallel c$ ) and in the  $ab$ -plane ( $B \parallel ab$ ) of the film.

Figure 6(a) presents the temperature-dependent zero magnetic field sheet resistance ( $R_S$ ) between 5 and 300 K for a 25-nm-thick unpatterned Sr<sub>3</sub>Ru<sub>2</sub>O<sub>7</sub> film and for two representative patterned Hall bar devices fabricated side-by-side on this same film after Van der Pauw measurements. The unpatterned Sr<sub>3</sub>Ru<sub>2</sub>O<sub>7</sub> film and devices show metallic behavior over the entire temperature range. At 5 K, the  $R_S$  is roughly a factor of 4 higher in unpatterned film than in Hall bar devices. The extracted residual resistivity ratio RRR, defined as  $\rho(300 \text{ K})/\rho(5 \text{ K})$ , is  $\text{RRR} \simeq 6.8$  for 25 nm-thick films. This value is consistent with reported resistivity data of MBE-grown Sr<sub>3</sub>Ru<sub>2</sub>O<sub>7</sub> films of similar thickness [10]. From the temperature dependence of the normalized resistances,  $R(T)/R(5 \text{ K})$ , at various applied  $B$ -field orientations, the measured temperature dependence is isotropic in the absence of an applied field, while enhanced scattering is observed for in-plane applied  $B$ -field of 5 T [see, Fig. S2 of the supplementary material]. This enhanced scattering near the metamagnetic field transition was observed in a strained Sr<sub>3</sub>Ru<sub>2</sub>O<sub>7</sub> films [10], and it has been attributed to field-controlled instabilities of the Fermi surface of Sr<sub>3</sub>Ru<sub>2</sub>O<sub>7</sub> [31].

Figures 6(b)-6(d) show the MR at several temperatures for the same unpatterned film and two Hall bar devices fabricated on the same sample after measurements in Van der Pauw geometry. The magnetoresistance is defined as  $\text{MR} = \left( \frac{R_{xx}(B) - R_{xx}(0)}{R_{xx}(0)} \right) \times 100$ , where  $R_{xx}(B)$  and  $R_{xx}(0)$  are the longitudinal resistance measured at a field  $B$  and at zero field, respectively. MR data were acquired with the  $B$ -field in out-of-plane direction ( $B \parallel c$ -axis,  $\theta = 0^\circ$ ), the excitation current being perpendicular to the

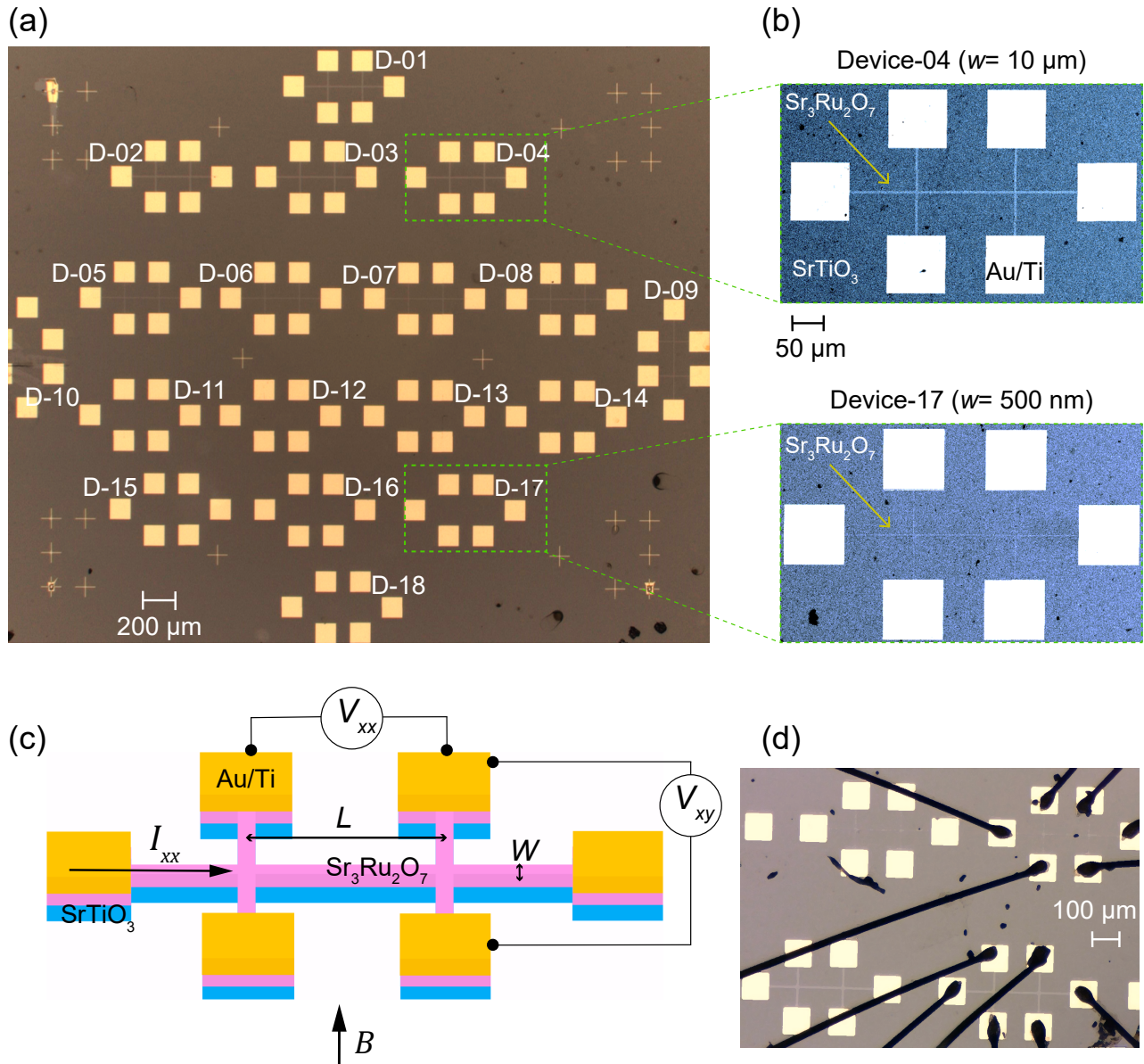


FIG. 5. **Device fabrication and measurement configuration.** (a) Optical micrograph image showing a top view of the whole  $\text{Sr}_3\text{Ru}_2\text{O}_7$  film on which several Hall bar devices of different channel widths ( $W$ ) were fabricated side-by-side on the same film. The channel widths are  $W = 10 \mu\text{m}$ ,  $5 \mu\text{m}$ ,  $1 \mu\text{m}$  and  $500 \text{nm}$  for Hall bar devices D-01 to D-04, D-05 to D-09, D-10 to D-14, and D-15 to D-18, respectively. (b) SEM images of representative Hall bar devices of  $W = 10 \mu\text{m}$  and  $500 \text{nm}$ . (c) Configuration of magnetotransport measurement for  $\text{Sr}_3\text{Ru}_2\text{O}_7$  Hall bar devices. The length ( $L$ ) between longitudinal voltage contacts is the same for all Hall bar devices in (a),  $L = 200 \mu\text{m}$ . (d) Photograph of  $\text{Sr}_3\text{Ru}_2\text{O}_7$  devices that are wire-bonded for magnetotransport measurements. Due to the limited number of available contacts on a chip carrier, only two devices on a sample could be bonded at once.

field ( $B \perp I$ ). No hysteresis loop was observed, which indicates that no intrinsic long-range ferromagnetic order occurs. Details on the analysis of MR data are discussed elsewhere [48–50]

For unpatterned films measured in Van der Pauw geometry at 5 K, a positive MR is measured at low magnetic fields together with a shallow change of slope slightly above 6 T [Fig. 6(b)]. As the temperature is increased further, this shallow slope at high  $B$ -field disappears and

MR data show quasi-quadratic field dependence. Positive MR with change of slope from a positive to a negative, resulting into a MR peak around 6 T, has been reported in thin  $\text{Sr}_3\text{Ru}_2\text{O}_7$  single crystal nanosheets measured at 500 mK with  $B \parallel c$ -axis [30]. The positive MR peak has been associated with the metamagnetic transition in  $\text{Sr}_3\text{Ru}_2\text{O}_7$  [27, 30]. For patterned Hall bar devices, a positive and quasi-quadratic field dependence MR is observed independent of temperature [Fig. 6(c)-6(d)]. We

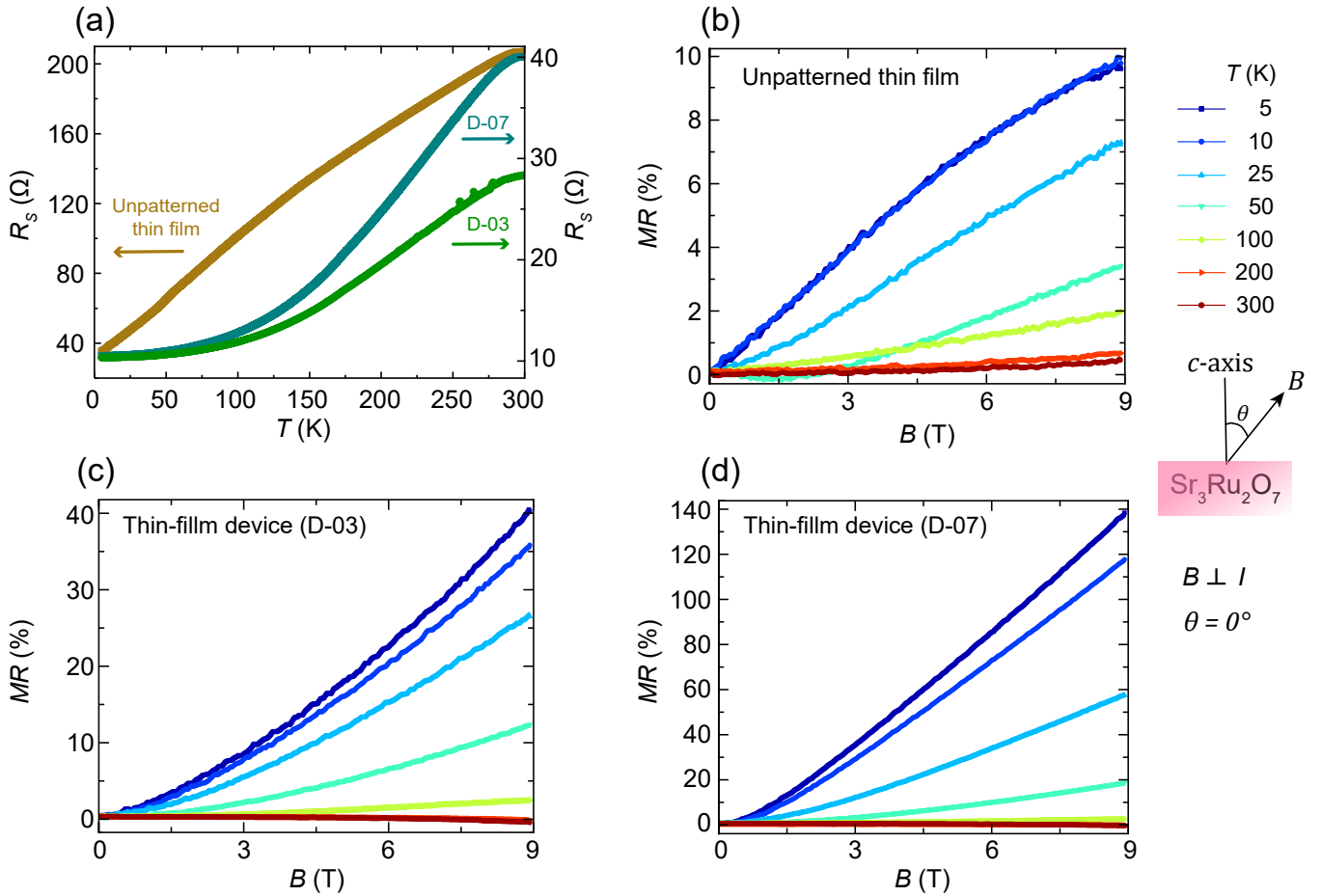


FIG. 6. **Magnetotransport characteristics of a  $\text{Sr}_3\text{Ru}_2\text{O}_7$  epitaxial film at various temperatures.** (a) Temperature dependence of the zero-field sheet resistance ( $R_S$ ) of a 25 nm-thick  $\text{Sr}_3\text{Ru}_2\text{O}_7$  film before device fabrication (unpatterned thin film), and the  $R_S$  of two representative patterned Hall bar devices (D-03 and D-07) fabricated on the same  $\text{Sr}_3\text{Ru}_2\text{O}_7$  film. The channel widths of D-03 and D-07 are 10  $\mu\text{m}$  and 5  $\mu\text{m}$ , respectively. (b) Magnetoresistance (MR) curves of a  $\text{Sr}_3\text{Ru}_2\text{O}_7$  film measured at various temperatures in the Van der Pauw geometry before device fabrication (unpatterned thin film), and for (c)-(d) patterned Hall bar thin-film devices fabricated on the same film after measurements in the Van der Pauw configuration. MR data were acquired with  $B \parallel c$ -axis,  $\theta = 0^\circ$  ( $\theta$  is the angle between the  $B$ -field and  $c$ -axis, as schematically illustrated in the right-side of the figure).

are not able to resolve a MR peak in these  $\text{Sr}_3\text{Ru}_2\text{O}_7$  films, because MR data were acquired only down to 5 K and up to 9 T. For  $\text{Sr}_3\text{Ru}_2\text{O}_7$  single crystals, a broad MR peak at 5 K was resolved only for MR data acquired up to 15 T [27].

The MR increases with decreasing temperature and it evolves into quasi-linear behavior in the high field limit. For the unpatterned  $\text{Sr}_3\text{Ru}_2\text{O}_7$  film, a maximum MR ( $T = 5$  K,  $B = 9$  T) of 10% is obtained [Fig. 6(b)]. However, Hall bar devices fabricated on this same film show large positive MR values of 40% and 140% for devices of channel widths of 10 and 5  $\mu\text{m}$ , respectively [Fig. 6(c)-6(d)]. The positive MR for  $B \parallel c$  is an indication of paramagnetic behavior of these films, which is consistent with known resistivity increase as magnetic field increases in most materials [51]. While for ferromagnets, MR is negative; for paramagnetic metals, the movement of carriers will be deflected under a Lorentz force, which increases

the probability of carrier scattering, thereby increasing the resistance.

For the same film characterized in Figure 6, we have performed angle dependence MR measurements at various temperatures. Figure 7(a) depicts representative MR data at 5 K for unpatterned  $\text{Sr}_3\text{Ru}_2\text{O}_7$  film. The MR data were acquired for  $\theta$  (the angle between the  $B$ -field and the  $c$ -axis of the sample) values of  $0^\circ$ ,  $45^\circ$  and  $90^\circ$ . As  $\theta$  increases from  $0^\circ$  to  $90^\circ$ , the MR undergoes a gradual transition from positive to negative. For  $\theta = 90^\circ$ , the MR is negative and it reaches a local minimum at a magnetic field of  $\simeq 5.8$  T, which is consistent with the in-plane metamagnetic transition reported for  $\text{Sr}_3\text{Ru}_2\text{O}_7$  single crystals [27, 28]. MR data of Hall bar device fabricated on the same film exhibit qualitatively similar switching behaviors from positive to negative MR as the magnetic field is applied from out-of-plane ( $B \parallel c$ -axis) to in-plane direction ( $B \parallel ab$ -plane) [see Fig. S3 of

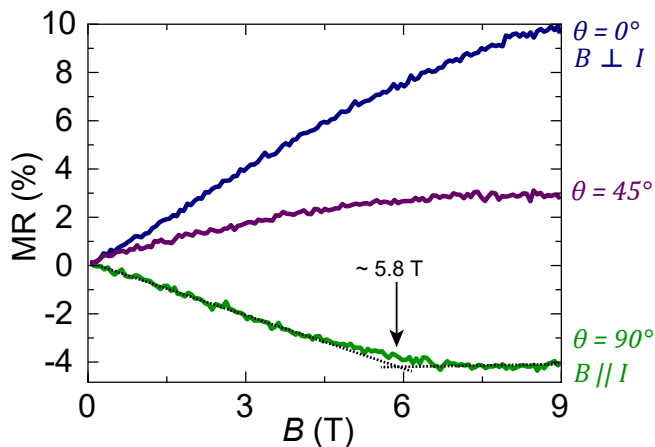


FIG. 7. **MR characteristics at different  $B$ -field orientation.** The MR data of unpatterned  $\text{Sr}_3\text{Ru}_2\text{O}_7$  film were measured at 5 K in the Van der Pauw geometry. Linear fits (black dotted lines) on the MR curve for  $\theta = 90^\circ$  indicate a change of slope at a magnetic field of  $\sim 5.8$  T.

the supplementary material]. A maximum negative MR ( $T = 5$  K,  $B = 9$  T,  $\theta = 90^\circ$ ) values of -4% and -70% are obtained for unpatterned film [Fig. 7(a)] and Hall bar device [Fig. S3], respectively.

The observation of a negative MR at  $\theta = 90^\circ$ , accompanied with a local minimum and shallow positive slope at high magnetic field, is attributed to the coexistence of short-range in-plane ferromagnetic order in the surface layer and metamagnetism in these films. The  $\text{Ru}^{4+}$  spin becomes aligned due to the applied magnetic field, thus spin-dependent scattering decreases, which gives rise to a negative MR. This observation is consistent with a recent magnetic field-controlled spectroscopic study that resolved in-plane ferromagnetism in  $\text{Sr}_3\text{Ru}_2\text{O}_7$  single crystals that is sensitive to the direction of applied magnetic field [52]. Furthermore, we conjecture that the high MR values in these films is due to spin fluctuations of the mobile electronic carriers when the material is under applied magnetic fields.

In summary, we have explored an approach to stabilize the epitaxy of  $\text{Sr}_3\text{Ru}_2\text{O}_7$  films by varying the substrate temperature and laser fluence in the PLD process, and investigated the magnetotransport trends in these epitaxial films. Structural characterizations of  $\text{Sr}_3\text{Ru}_2\text{O}_7$  films prepared at optimal growth conditions confirm that these films are epitaxially oriented and nearly phase pure. Resistivity measurements of  $\text{Sr}_3\text{Ru}_2\text{O}_7$  films and

Hall bar devices exhibit characteristic metallic behavior. The magnetization characteristics of the films show no intrinsic ferromagnetic transition over the entire measured temperature range. These films exhibit a qualitatively similar MR behavior as previously reported for bulk single crystals and strained epitaxial films, specifically positive MR for the magnetic field applied along the  $c$ -axis and negative MR for the magnetic field applied along the  $ab$ -plane of the film. However, we achieve unprecedented large magnetoresistance values up to 40% and 140% in unpatterned  $\text{Sr}_3\text{Ru}_2\text{O}_7$  films and Hall bar devices, respectively. This provides an opportunity to explore more the physics of  $\text{Sr}_3\text{Ru}_2\text{O}_7$ -based electronic devices for the realization and modulation of novel emergent phenomena (*e.g.*, nematic phase and non-Fermi-liquid behavior) in submicrometer devices. Based on these results, future directions are expected to focus on the investigation of magnetotransport properties of quantum structures (*e.g.*, nonwires and quantum dots) patterned on epitaxial  $\text{Sr}_{n+1}\text{Ru}_n\text{O}_{3n+1}$  films, as well as on nanoscale devices fabricated side-by-side on the same film in which magnetotransport properties can be modulated through quantum size effects and applied electric fields.

## Supplementary Material

See the supplementary material for additional microstructural characterizations using TEM and magnetotransport measurements of epitaxial  $\text{Sr}_3\text{Ru}_2\text{O}_7$  films.

## Acknowledgments

The authors acknowledge technical support from Sarah Parks.

P. Ngabonziza acknowledges startup funding from the College of Science and the Department of Physics & Astronomy at Louisiana State University.

A. Scheid acknowledges the invaluable assistance of Tobias Heil for his support with STEM examinations, and Y. Eren Suyolcu for his exceptional efforts in coordinating the STEM examinations and interpreting the results.

A. Scheid and P. van Aken acknowledge funding from the European Union's Horizon 2020 research and innovation programme under Grant Agreement No.823717-ESTEEM3.

## Data Availability

The data that support the findings of this study are available from the corresponding author upon reasonable request.

- [1] A. Chronister, A. Pustogow, N. Kikugawa, D. A. Sokolov, F. Jerzembeck, C. W. Hicks, A. P. Mackenzie, E. D. Bauer, and S. E. Brown, *PNAS* **118**, 25 (2021).
- [2] Z. Ali, M. Saghayezhian, Z. Wang, A. O'Hara, D. Shin, W. Ge, Y. T. Chan, Y. Zhu, W. Wu, S. T. Pantelides, and J. Zhang, *npj Quantum Mater.* **7**, 108 (2022).

- [3] E. Dagotto, *Science* **309**, 257 (2005).
- [4] S. A. Grigera, R. S. Perry, A. J. Schofield, M. Chiao, S. R. Julian, G. G. Lonzarich, S. I. Ikeda, Y. Maeno, A. J. Millis, and A. P. Mackenzie, *Science* **294**, 329 (2001).
- [5] Y. Maeno, H. Hashimoto, K. Yoshida, S. Nishizaki, T. Fujita, J. G. Bednorz, and F. Lichtenberg, *Nature*

- (London) **372**, 532 (1994).
- [6] A. P. Mackenzie and Y. Maeno, *Rev. Mod. Phys.* **75**, 657 (2003), and references therein.
- [7] S. A. Kivelson, A. C. Yuan, B. Ramshaw, and R. Thomale, *npj Quantum Mater.* **5**, 43 (2020).
- [8] R. A. Borzi, S. A. Grigera, J. Farrell, R. S. Perry, S. J. S. Lister, S. L. Lee, D. A. Tennant, Y. Maeno, and A. P. Mackenzie, *Science* **315**, 214 (2007).
- [9] S. Raghu, A. Paramakanti, E. A. Kim, R. A. Borzi, S. A. Grigera, A. P. Mackenzie, and S. A. Kivelson, *Phys. Rev. B* **79**, 214402 (2009).
- [10] P. B. Marshall, K. Ahadi, H. Kim, and S. Stemmer, *Phys. Rev. B* **97**, 155160 (2018).
- [11] P. Gegenwart, F. Weickert, M. Garst, R. S. Perry, and Y. Maeno, *Phys. Rev. Lett.* **96**, 136402 (2006).
- [12] Y. J. Jo, L. Balicas, N. Kikugawa, E. S. Choi, K. Storr, M. Zhou, and Z. Q. Mao, *Phys. Rev. B* **75**, 094413.
- [13] E. Carleschi, B. P. Doyle, R. Fittipaldi, V. Granata, A. M. Strydom, M. Cuoco, and A. Vecchione, *Phys. Rev. B* **90**, 205120 (2014).
- [14] D. Fobes, T. J. Liu, Z. Qu, M. Zhou, J. Hooper, M. Salamon, and Z. Q. Mao, *Phys. Rev. B* **81**, 172402 (2010).
- [15] P. Ngabonziza, J. D. Denlinger, A. V. Fedorov, G. Cao, J. W. Allen, G. Gebreyesus, and R. M. Martin, *arXiv:2305.07222* (2023).
- [16] G. Koster, L. Klein, W. Siemons, G. Rijnders, J. S. Dodge, C.-B. Eom, D. H. A. Blank, and M. R. Beasley, *Rev. Mod. Phys.* **84**, 253 (2012), and references therein.
- [17] S. Hahn, B. Sohn, M. Kim, J. R. Kim, S. Huh, Y. Kim, W. Kyung, M. Kim, D. Kim, Y. Kim, T. W. Noh, J. H. Shim, and C. Kim, *Phys. Rev. Lett.* **127**, 256401 (2021).
- [18] M. Kim and B. I. Min, *Phys. Rev. B* **91**, 205116 (2015).
- [19] H. Boschker, T. Harada, T. Asaba, R. Ashoori, A. V. Boris, H. Hilgenkamp, C. R. Hughes, M. E. Holtz, L. Li, D. A. Muller, H. Nair, P. Reith, X. Renshaw Wang, D. G. Schlom, A. Soukiassian, and J. Mannhart, *Phys. Rev. X* **9**, 011027 (2019).
- [20] H. P. Nair, J. P. Ruf, N. J. Schreiber, L. Miao, M. L. Grandon, D. J. Baek, B. H. Goodge, J. P. C. Ruff, L. F. Kourkoutis, K. M. Shen, and D. G. Schlom, *APL Mater.* **6**, 101108 (2018).
- [21] Y. Fang, H. P. Nair, L. Miao, B. Goodge, N. J. Schreiber, J. P. Ruf, L. F. Kourkoutis, K. M. Shen, D. G. Schlom, and B. J. Ramshaw, *Phys. Rev. B* **104**, 045152 (2021).
- [22] P. Ngabonziza, Y. Wang, P. A. van Aken, J. Maier, and J. Mannhart, *Adv. Mater.* **33**, 2007299 (2021).
- [23] S. Kaneta-Takada, Y. K. Wakabayashi, Y. Krockenberger, T. Nomura, Y. Kohama, S. A. Nikolaev, H. Das, H. Irie, K. Takiguchi, S. Ohya, M. Tanaka, Y. Taniyasu, and H. Yamamoto, *npj Quantum Mater.* **7**, 102 (2022).
- [24] K. Takiguchi, Y. K. Wakabayashi, H. Irie, Y. Krockenberger, T. Otsuka, H. Sawada, S. A. Nikolaev, H. Das, M. Tanaka, Y. Taniyasu, and H. Yamamoto, *Nat. Commun.* **11**, 4969 (2020).
- [25] W. Tian, J. H. Haeni, D. G. Schlom, E. Hutchinson, B. L. Sheu, M. M. Rosario, P. Schiffer, Y. Liu, M. A. Zurbuchen, and X. Q. Pan, *Appl. Phys. Lett.* **90**, 022507 (2007).
- [26] S.-I. Ikeda, Y. Maeno, S. Nakatsuji, M. Kosaka, and Y. Uwatoko, *Phys. Rev. B* **62**, R6089 (2000).
- [27] R. S. Perry, L. M. Galvin, S. A. Grigera, L. Capogna, A. J. Schofield, A. P. Mackenzie, M. Chiao, S. R. Julian, S. I. Ikeda, S. Nakatsuji, Y. Maeno, and C. Pfleiderer, *Phys. Rev. Lett.* **86**, 2661 (2001).
- [28] E. Ohmichi, Y. Yoshida, S. I. Ikeda, N. V. Mushunikov, T. Goto, and T. Osada, *Phys. Rev. B* **67**, 024432 (2003).
- [29] S. A. Grigera, P. Gegenwart, R. A. Borzi, F. Weickert, A. J. Schofield, R. S. Perry, T. Tayama, T. Sakakibara, Y. Maeno, A. G. Green, and A. P. Mackenzie, *Science* **306**, 1154 (2004).
- [30] W. Chu, N. Wang, Y. Liu, Y. Wang, G. Liu, Y. Han, N. Hao, Z. Qu, J. Yang, F. Xue, Z. Mao, and M. Tian, *Phys. Rev. B* **102**, 195119 (2020).
- [31] A. Tamai, M. P. Allan, J. F. Mercure, W. Meevasana, R. Dunkel, D. H. Lu, R. S. Perry, A. P. Mackenzie, D. J. Singh, Z.-X. Shen, and F. Baumberger, *Phys. Rev. Lett.* **101**, 026407 (2008).
- [32] V. Shaginyan, A. Msezane, K. Popov, J. Clark, M. Zverev, and V. Khodel, *Phys. Lett. A* **377**, 2800 (2013).
- [33] P. Ngabonziza, E. Carleschi, V. Zabolotnyy, A. Taleb-Ibrahimi, F. Bertran, R. Fittipaldi, V. Granata, M. Cuoco, A. Vecchione, and B. P. Doyle, *Sci. Rep.* **10**, 21062.
- [34] G. Gebreyesus, P. Ngabonziza, J. Nagura, N. Seriani, O. Akin-Ojo, and R. M. Martin, *Phys. Rev. B* **105**, 165119 (2022).
- [35] I. Benedičič, M. Naritsuka, L. C. Rhodes, C. Trainer, Y. Nanao, A. B. Naden, R. Fittipaldi, V. Granata, M. Lettieri, A. Vecchione, and P. Wahl, *Phys. Rev. B* **106**, L241107 (2022).
- [36] E. Fradkin, S. A. Kivelson, M. J. Lawler, J. P. Eisenstein, and A. P. Mackenzie, *Annu. Rev. Condens. Matter Phys.* **1**, 153 (2010), and references therein.
- [37] J. Hooper, M. Zhou, Z. Mao, R. Perry, and Y. Maeno, *Phys. Rev. B* **72**, 134417 (2005).
- [38] W. Braun, M. Jäger, G. Laskin, P. Ngabonziza, W. Voesch, P. Wittlich, and J. Mannhart, *APL Mater.* **8**, 071112 (2020).
- [39] A stoichiometric PLD target of  $\text{Sr}_3\text{Ru}_2\text{O}_7$  was obtained from Toshiba Manufacturing Co., Ltd. <http://www.material-sys.com/> (accessed: September 2023). Using a stoichiometric  $\text{SrRuO}_3$  PLD target obtained from the same supplier, we also made control films of  $\text{SrRuO}_3$  ().
- [40] Q. Huang, J. W. Lynn, R. W. Erwin, J. Jarupatrakorn, and R. J. Cava, *Phys. Rev. B* **58**, 8515 (1998).
- [41] N. Aso, Y. Uwatoko, H. Kimura, Y. Noda, Y. Yoshida, S.-I. Ikeda, and S. Katano, *J. Phys.: Condens. Matter* **17**, S3025 (2005).
- [42] H. Shaked, J. Jorgensen, O. Chmaissem, S. Ikeda, and Y. Maeno, *J. Solid State Chem.* **154**, 361 (2000).
- [43] Since  $\text{SrRuO}_3$  has the most thermodynamically stable phase in the  $\text{Sr}_{n+1}\text{Ru}_n\text{O}_{3n+1}$  series [53], control films of  $\text{SrRuO}_3$  [39] were used to trace possible inter-growth phases and change of stability in  $\text{Sr}_3\text{Ru}_2\text{O}_7$  films. Control samples of  $\text{SrRuO}_3$  were grown at a substrate temperature of  $680^\circ\text{C}$  and laser fluence of  $2 \text{ J}\cdot\text{cm}^{-2}$  ().
- [44] J. H. Haeni, C. D. Theis, D. G. Schlom, W. Tian, X. Q. Pan, H. Chang, I. Takeuchi, and X.-D. Xiang, *Appl. Phys. Lett.* **78**, 3292 (2001).
- [45] E. E. Fleck, M. R. Barone, H. P. Nair, N. J. Schreiber, N. M. Dawley, D. G. Schlom, B. H. Goodge, and L. F. Kourkoutis, *Nano Lett.* **22**, 10095 (2022).
- [46] W. Tian, X. Q. Pan, J. H. Haeni, and D. G. Schlom, *J. Mater. Res.* **16**, 2013 (2001).
- [47] G. Laskin, H. Wang, H. Boschker, W. Braun, V. Srot, P. A. van Aken, and J. Mannhart, *Nano Lett.* **19**, 1131

- (2019).
- [48] M. P. Stehno, P. Ngabonziza, H. Myoren, and A. Brinkman, *Adv. Mater.* **32**, 1908351 (2020).
- [49] P. Ngabonziza, *Nanotechnology* **33**, 192001 (2022).
- [50] P. Ngabonziza, Y. Wang, and A. Brinkman, *Phys. Rev. Mater.* **2**, 044204 (2018).
- [51] R. Niu and W. K. Zhu, *J. Condens. Matter Phys.* **34**, 113001 (2021).
- [52] M. Naritsuka, I. Benedičič, L. C. Rhodes, C. A. Marques, C. Trainer, Z. Li, A. C. Komarek, and P. Wahl, *PNAS* **120**, e2308972120 (2023).
- [53] H. P. Nair, Y. Liu, J. P. Ruf, N. J. Schreiber, S.-L. Shang, D. J. Baek, B. H. Goodge, L. F. Kourkoutis, Z.-K. Liu, K. M. Shen, and D. G. Schlom, *APL Mater.* **6**, 046101 (2018).

## Supplementary Information:

### Magnetotransport Trends in Epitaxial Films and Electronic Devices of Correlated Layered Ruthenate $\text{Sr}_3\text{Ru}_2\text{O}_7$

Prosper Ngabonziza,<sup>1,2,\*</sup> Anand Sharma,<sup>1</sup> Anna Scheid,<sup>3</sup> Sethulakshmi Sajeev,<sup>1</sup>  
Peter A. van Aken,<sup>3</sup> and Jochen Mannhart<sup>3</sup>

<sup>1</sup>*Department of Physics & Astronomy, Louisiana State University, Baton Rouge, LA 70803, USA*

<sup>2</sup>*Department of Physics, University of Johannesburg, P.O. Box 524, Auckland Park 2006, Johannesburg, South Africa*

<sup>3</sup>*Max Planck Institute for Solid State Research, Heisenbergstr. 1, 70569 Stuttgart, Germany*

#### Microstructural Characterization of Epitaxial $\text{Sr}_3\text{Ru}_2\text{O}_7$ Films

Scanning transmission electron microscopy (STEM) and electron energy loss spectroscopy (EELS) investigations were performed using a Cs-probe-corrected JEOL JEM-ARM200F. Using STEM, we have performed a detailed mi-

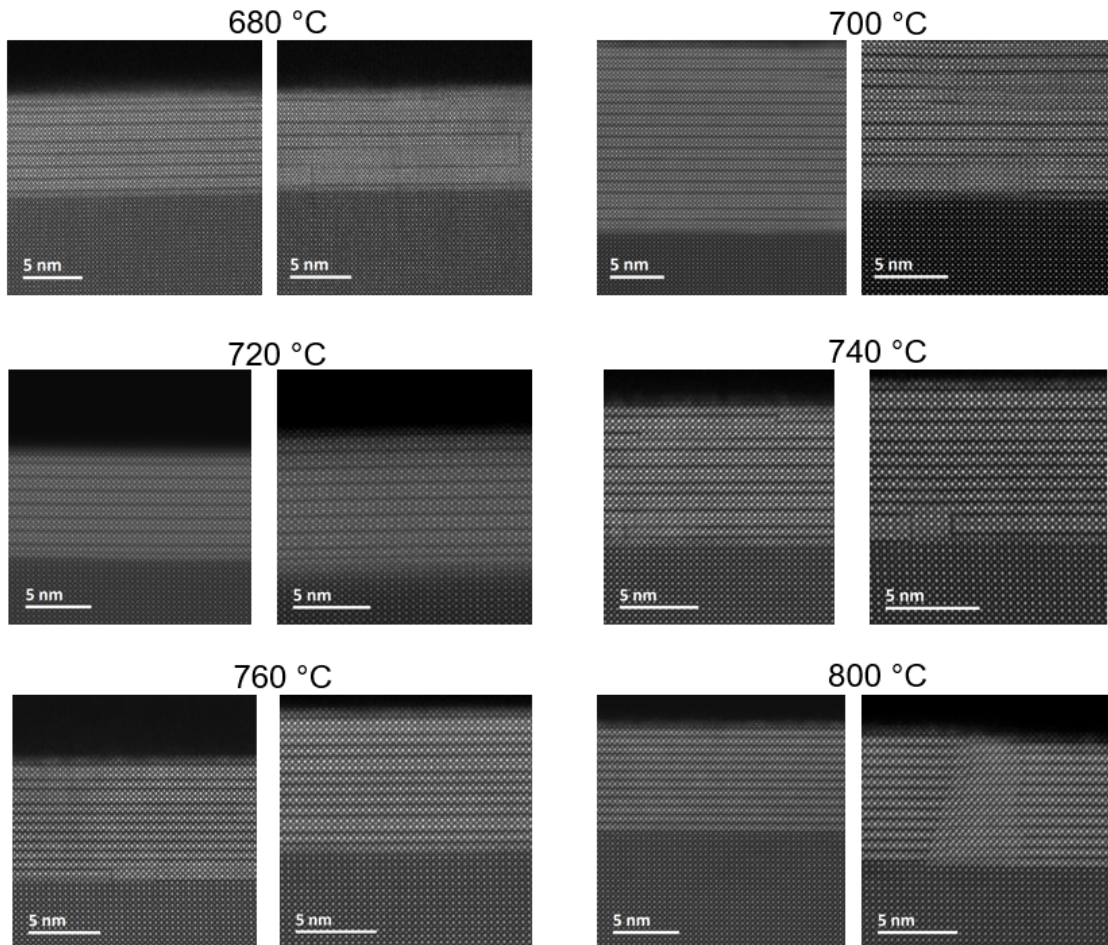


FIG. S1. STEM images of  $\text{Sr}_3\text{Ru}_2\text{O}_7$  films grown on (100)-oriented  $\text{SrTiO}_3$  substrates at various substrate temperatures.

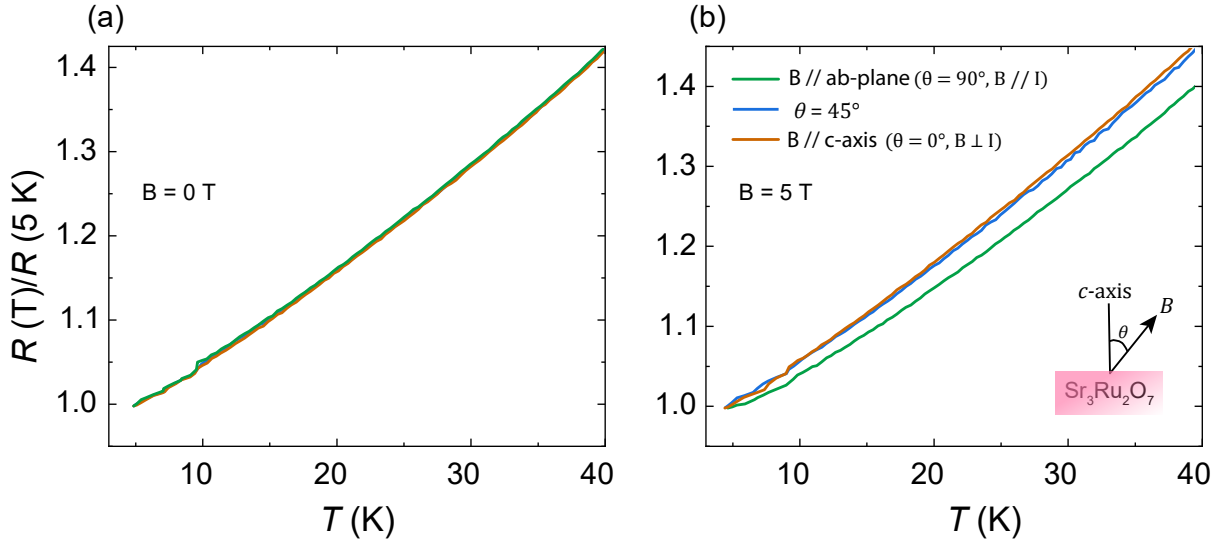


FIG. S2. Normalized sheet resistance of epitaxial  $\text{Sr}_3\text{Ru}_2\text{O}_7$  films with an applied magnetic field of (a) 0 T and (b) 5 T. The applied field  $B$  is along various directions:  $B$ -field parallel to the  $c$ -axis ( $\theta = 0^\circ$ ) with the current perpendicular to the field ( $B \perp I$ ),  $B$ -field parallel to the  $ab$ -plane ( $\theta = 90^\circ$ ) with the current parallel to the field ( $B \parallel I$ ), and in the configuration of the  $B$ -field applied at an angle of  $\theta = 45^\circ$  with respect to the  $c$ -axis.

crostructural characterization of  $\text{Sr}_3\text{Ru}_2\text{O}_7$  films grown by pulsed laser deposition (PLD) at different substrate temperature. To improve the signal-to-noise ratio of the Electron energy-loss spectroscopy (EELS) elemental mapping of  $\text{Sr}_3\text{Ru}_2\text{O}_7/\text{SrTiO}_3$  interface [see, Fig. 3(d) of the main text], we used principal component analysis including 20 principal components. Figure S1 depicts representative STEM images in  $[100]$  zone axis orientation for  $\text{Sr}_3\text{Ru}_2\text{O}_7$  films grown at various substrate temperatures ranging from  $680^\circ\text{C}$  to  $800^\circ\text{C}$ . At a substrate temperature of  $680^\circ\text{C}$ , the films exhibit some intergrowth and noticeable defects. As the growth temperature increases, intergrowth and structural defects reduces and at  $720^\circ\text{C}$ , films exhibit a dominant  $\text{Sr}_3\text{Ru}_2\text{O}_7$  phase with no noticeable defects in the scanned areas. The optimal substrate temperature of  $\text{Sr}_3\text{Ru}_2\text{O}_7$  films grown by PLD on  $\text{SrTiO}_3$  substrates was found to be around  $720^\circ\text{C}$ . Increasing further the substrate temperature above  $720^\circ\text{C}$ , the films exhibit increased defect density and considerable inter-growths of other  $n$  members of the  $\text{Sr}_{n+1}\text{Ru}_n\text{O}_{3n+1}$  Ruddlesden-Popper (RP) phases are observed. In general we observe a trend that for lower growth temperatures, the  $n \geq 2$  RP phases predominate in the parasitic phases, whereby this fraction decreases with increasing temperature until finally at higher substrate temperatures ( $800^\circ\text{C}$ ), the films are dominantly  $n = 1$  RP phase and in the scanned areas they exhibit defects running across the film from the interface between substrate and the film.

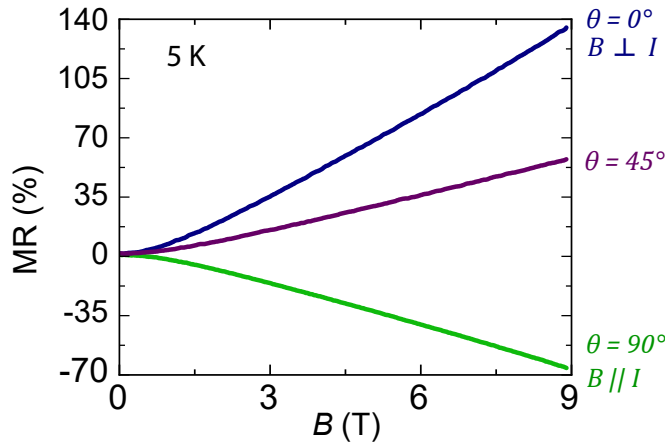


FIG. S3. The MR data at different orientation of applied magnetic field of a patterned Hall bar device fabricated on the same film presented in Fig. 7 of the main text. Device fabrication was done after measurements in the Van der Pauw configuration.

Figure S2 depicts the temperature dependence of the normalized sheet resistance,  $R(T)/R(5\text{ K})$ , of a representative 25-nm-thick  $\text{Sr}_3\text{Ru}_2\text{O}_7$  film acquired with applied magnetic field of 0 T [Fig. S2(a)] and 5 T [Fig. S2(b)]. Data were taken with the magnetic field applied along the  $c$ -axis ( $B \parallel c$ -axis), along the  $ab$ -plane ( $B \parallel ab$ -plane), and the field at an angle of  $45^\circ$  with respect to the  $c$ -axis. In the absence of an applied magnetic field, the normalized sheet resistance show similar characteristics with the curves nearly overlapping on top of one another [Fig. S2(a)]. At the critical magnetic field of 5 T, enhanced scattering is observed when the excitation current is parallel to applied magnetic field [Fig. S2(b)]. Figure S3 depicts MR data at 5 K for a patterned  $\text{Sr}_3\text{Ru}_2\text{O}_7$  Hall bar device (D-07 of channel width of  $5\mu\text{m}$ ). The MR data were acquired for  $\theta$  (the angle between the  $B$ -field and  $c$ -axis, as schematically illustrated in the inset of Fig. S2) values of  $\theta = 0^\circ, 45^\circ$ , and  $90^\circ$ .